crystals

MDPI

Article

Synthesis and Luminescence Properties of Green-to-Red Color-Tunable Upconverting $K_2Gd(PO_4)(WO_4)$:Yb^{3+},Tb^{3+},Eu^{3+} Phosphors

Julija Grigorjevaite * and Arturas Katelnikovas *

Institute of Chemistry, Faculty of Chemistry and Geosciences, Vilnius University, Naugarduko 24, LT-03225 Vilnius, Lithuania

* Correspondence: julija.grigorjevaite@chgf.vu.lt (J.G.); arturas.katelnikovas@chf.vu.lt (A.K.)

Abstract: Scientists are increasingly interested in new inorganic luminescence materials that could be excited with near-infrared (NIR) radiation. These materials can be used as luminescent thermometers, bio-imaging agents, anti-counterfeiting pigments, etc. In this manuscript, we report the synthesis and investigation of optical properties of two series of $K_2Gd(PO_4)(WO_4)$:20%Tb^{3+} (KGPW): the first, KGPW:20%Tb^{3+} doped with 1–20% Eu^{3+}, and the second, KGPW:10%Yb^{3+},20%Tb^{3+} doped with 1–20% Eu^{3+}. The phase-pure specimens were prepared using a solid-state synthesis method. Down-shifting and upconversion luminescence studies have been performed using 340 and 980 nm excitation, respectively. For upconversion emission luminescence, Yb^{3+} ions were used as sensitizers in the KGPW phosphors. In these phosphors, Yb^{3+} ions absorb the 980 nm radiation and transfer the energy to Tb^{3+} ions. At his point, Tb^{3+} ions either emit themselves or transfer part or all of their energy to Eu^{3+} ions. It was observed that the emission color of the synthesized phosphors could be successfully tuned from the green to red by varying the Tb/Eu concentration ratio regardless of the 340 or 980 nm excitation. Such color change proves that one luminescent material (KGPW) can provide three colors (i.e., green, orange, and red). Herein, the optical properties, such as reflection, down-shifting excitation and emission spectra, upconversion emission spectra, fluorescence lifetime, thermal quenching, color coordinates, and quantum efficiency, were studied using steady-state and kinetic spectroscopy.

Keywords: down-shifting; upconversion; thermal quenching; energy transfer; color coordinates

check for updates

Citation: Grigorjevaite, J.; Katelnikovas, A. Synthesis and Luminescence Properties of Green-to-Red Color-Tunable Upconverting $K_2Gd(PO_4)(WO_4)$:Yb^{3+},Tb^{3+},Eu^{3+} Phosphors. *Crystals* **2023**, *13*, 479. https://doi.org/10.3390/cryst13030479

Academic Editor: David Stratos

Received: 15 February 2023
Revised: 3 March 2023
Accepted: 8 March 2023
Published: 10 March 2023

Copyright: © 2023 by the authors. Licensee MDPI, Basel, Switzerland. This article is an open access article distributed under the terms and conditions of the Creative Commons Attribution (CC BY) license (https://creativecommons.org/licenses/by/4.0/).

1. Introduction

In modern times, luminescent materials are still engaging due to their range of applications and wide variety of fields to potentially be applied to. Inorganic luminescent materials doped with trivalent lanthanide ions (RE^{3+}) are applied in solar cells [1], scintillators [2], light-emitting diodes [3], lasers [4], upconverting materials [5], security pigments [6], nanoscale optical writing [7], nanoscopy [8], etc. When RE^{3+} ions are introduced into suitable host matrices, partly forbidden f-f transitions become weakly allowed, and doped materials show photoluminescence properties. Thus, photoluminescence could be observed in two ways: down-shifting (DS) and upconversion (UC). When materials are excited with UV radiation, DS is observed. UC is a process wherein materials are excited with low-energy photons, commonly from laser excitation, and emit photons with higher-energy. Upconverting materials consist of a host doped with sensitizer and activator ions [9]. The well-known, widely used and reviewed sensitizer/activator pairs are Yb/Ho, Yb/Er, and Yb/Tm. The Yb^{3+} energy level structure is rather simple. It consists of only two energy levels: $^2F_{7/2}$ (ground state) and $^2F_{5/2}$ (excited state). The energy of the excited level matches well with the f-f energy levels of other RE^{3+} ions. The Yb/Tb sensitizer/activator pair is not widely studied, giving an opportunity to find novel UC phosphors. The excited state of

Yb^{3+} ($^2F_{5/2}$) overlaps with Tb^{3+} excited states ($^5D_2$ and $^5D_4$), allowing energy transfer from Yb^{3+} to Tb^{3+}.

Up until now, the most efficient UC lattice is still $NaYF_4$ [10]; this particular host is broadly discussed [11–14]. This host lattice has already been known for five decades, even though the synthesis of phase-pure $NaYF_4$ is still challenging. Usually, $NaYF_4$ synthesis yields two phases (hexagonal β–phase and cubic α–phase), and the synthesis of such nanoparticles requires a large amount of organic solvents [15,16]. For this reason, novel inorganic UC materials have received more attention.

The Yb/Tb/Eu system is the new alternative for the red-emitting Yb/Er sensitizer/activator pair and could possess a longer luminescence lifetime [17]. The upconverting materials possessing Tb^{3+} and Eu^{3+} allow the green/red emission ratio to change in the same matrix. Energy levels of Yb^{3+} do not overlap with Eu^{3+} energy levels. Due to this mismatch in energy levels, energy cannot be transferred from Yb^{3+} to Eu^{3+} directly. On the other hand, Tb^{3+} and Eu^{3+} energy levels overlap perfectly, and energy is transferred by a $Yb^{3+} \rightarrow Tb^{3+} \rightarrow Eu^{3+}$ mechanism [18–20]. The excited state of Tb^{3+} ($^5D_4$) has a similar energy to the $^5D_0$ level of Eu^{3+} ions. In this system, Tb^{3+} plays the role of the bridge between Yb^{3+} and Eu^{3+} ions. Thus, this mechanism allows the achievement of a color-tunable emission by changing the Eu^{3+} concentration in the samples.

There are many reasons why Eu^{3+} upconversion is worth analyzing [21,22]. The main reason is that $Yb^{3+}/Tb^{3+}/Eu^{3+}$ has not been widely studied yet and that gives us an opportunity to find new information about this system and the upconversion mechanism. Furthermore, the long luminescence lifetime of Eu^{3+} ions could be interesting for bio-imaging processes, using the Yb → Tb → Eu energy transfer mechanism [17]. Thus, the synthesized materials could be used as a red solid-state laser based on upconversion luminescence [23].

Tb^{3+} and Eu^{3+} ions are well known for their high emission efficiency related to the largest energy gap between emitting states and lower lying ^7F_J (J = 0, 1, 2, 3, 4, 5, 6, and 7) within lanthanides. Therefore, it is very interesting to study this UC system. For a better understanding, excitation and emission lines together with energy transfer are represented in fragments of Tb^{3+}, Eu^{3+}, and Yb^{3+} in Dieke's diagram (see Figure 1). Tb^{3+} is directly excited with a 340 nm excitation wavelength, and the $^7F_6$ energy level is excited to $^5D_2$ and then transferred two ways: (1) the energy relaxes to $^5D_3$, $^5G_6$, or $^5D_4$ and emits radiatively; and (2) the energy from $^5D_2$ or $^5D_4$ is transferred to Eu^{3+} and emits from $^5D_0$ to $^7F_{4;2;1}$ energy levels. For the upconversion optical property investigation, ions should be excited with a laser. For this reason, Yb^{3+} ions were incorporated in the matrix. The Yb^{3+} absorbs the laser radiation via the $^2F_{7/2} \rightarrow {}^2F_{5/2}$ transition and transfers it to Tb^{3+} which emits itself and transfers the energy further to Eu^{3+}. The energy from Yb^{3+} could not be transferred directly to Eu^{3+} ions as was confirmed by the emission spectra of the KGPW:10%Yb^{3+},20%Eu^{3+} sample when the sample was exposed to 980 nm laser radiation (please refer to Figure S1 see Supplementary Materials).

The KGPW host was extensively studied in our previous work. We have shown that the KGPW host is suitable for traditional upconversion pairs such as Yb/Er [24], Yb/Ho [25], and Yb/Tm [26]. The obtained upconverting materials showed emission in red, green/red, and blue/deep-red spectral areas, respectively. Herein, we investigate a more difficult system in the same host where three ions are involved in the upconversion process. The main aim of this work was to obtain new inorganic materials with tunable emission from the green-to-red spectral range under 340 and 980 nm excitation. For this reason, the KGPW:20%Tb^{3+} and KGPW:10%Yb^{3+},20%Tb^{3+} doped with 1–20% Eu^{3+} were synthesized using the solid-state reaction method at a fairly low temperature (873 K). The KGPW doped with all three rare-earth elements has not been synthesized before. This novel investigation could be interesting for understanding the Yb-Tb-Eu upconversion mechanism. The morphological and optical properties were investigated. The given data will include XRD, SEM, reflection, excitation, and emission spectra at room temperature and a 77–500 K interval, photoluminescence lifetimes, quantum efficiencies, and CIE 1931

color coordinates. Green (Tb^{3+}) and red (Eu^{3+}) luminescence can be obtained within the same compound at the same excitation wavelength by exciting Tb^{3+} directly and Eu^{3+} indirectly. The ration of green/red luminescence can be changed by varying the Eu^{3+} concentration. Herein, we will initially discuss the interaction between Tb^{3+} and Eu^{3+} ions when both are introduced into KGPW and KGPW:10%Yb^{3+} host matrices.

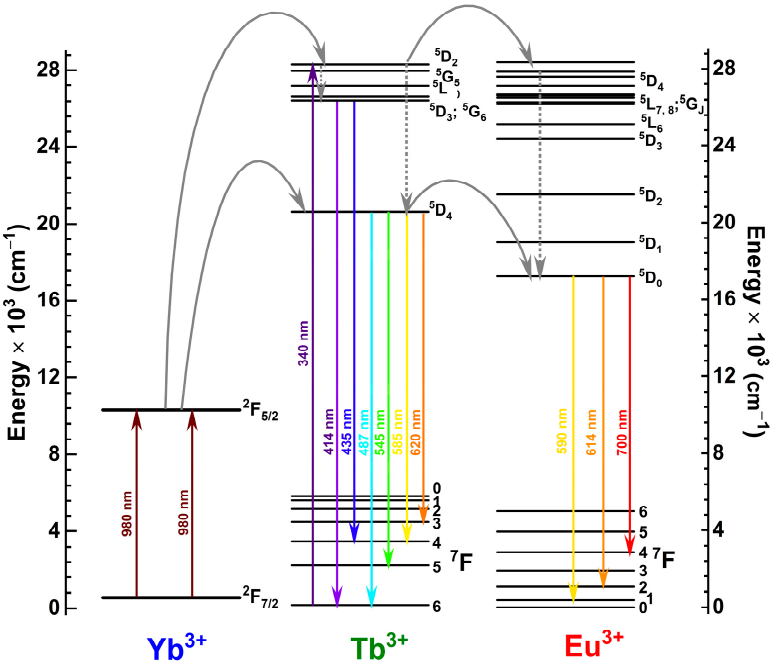

Figure 1. Schematic energy level diagram of energy transitions in Yb^{3+}, Tb^{3+}, and Eu^{3+} ions.

2. Materials and Methods

The samples were synthesized by the conventional solid-state reaction method according to our previous work [3,6]. The stoichiometric amounts of raw materials Gd_2O_3 (99.99% Tailorlux, Münster, Germany), K_2CO_3 (99+% Acros Organics, Geel, Belgium), $NH_4H_2PO_4$ (99% Reachem, Bratislava, Slovakia), WO_3 (99+% Acros Organics, Geel, Belgium), Eu_2O_3 (99.99% Tailorlux, Münster, Germany), Tb_4O_7 (99.99% Tailorlux, Münster, Germany), and Yb_2O_3 (99.99% Alfa Aesar, Haverhill, MA, USA) were weighed and mixed in an agate mortar using a few milliliters of acetone to ease the homogenization. The starting materials were ground with an agate pestle until all acetone evaporated. Subsequently, the blended materials were placed into the porcelain crucible and annealed three times at 873 K for 10 h in air. The powders were reground after each annealing step. The Eu^{3+} concentration in the KGPW:20%Tb^{3+} and KGPW:10%Yb^{3+},20%Tb^{3+} compounds were 1%, 2.5%, 5%, 10%, and 20%. The phase purity of the synthesized samples was checked using a Rigaku MiniFlexII (Rigaku, Tokyo, Japan) X-ray diffractometer working in a Bragg–Brentano focusing geometry. SEM images were taken using a FE-SEM Hitachi SU-70 (Hitachi, Tokyo, Japan) scanning electron microscope. Reflection, excitation, and emission spectra were recorded using modular a Edinburgh Instruments FLS980 spectrometer (Edinburgh Instruments, Livingston, UK) equipped with a 450 W Xe lamp and 980 nm emitting laser (MDL-III-980-1W) (Changchun New Industries Optoelectronics Tech. Co., Ltd., Changchun, P.R. China) as the excitation sources. The temperature-dependent measurements were performed on the same spectrometer equipped with a cryostat "MicrostatN" (77–500 K temperature range) from Oxford Instruments (Oxford Instruments, Abingdon, UK). The detailed measurement settings are reported in the supporting information file (please refer to Tables S1–S4).

3. Results and Discussion

3.1. Structural Analysis

The XRD patterns of the prepared samples are given in Figure S2. The patterns of the samples match well with the reference pattern of $K_2Bi(PO_4)(WO_4)$ (PDF4+ (ICDD) 04-013-4256). As expected, KGPW adopts the same orthorhombic crystal structure with the *Ibca* (#73) space group as $K_2Bi(PO_4)(WO_4)$ does. Due to the similar ionic radii, Gd^{3+} (1.053 Å) successfully replaces Bi^{3+} (1.17 Å) in the host matrix [27]. Ionic radii of Yb^{3+} (0.985 Å), Eu^{3+} (1.066 Å), and Tb^{3+} (1.04 Å) are very similar to the Gd^{3+} ionic radius; therefore, the single-phase KGPW compounds formed regardless the concentration of the dopant ions.

To calculate the unit cell parameters of the synthesized compounds, Rietveld refinement of the XRD patterns was performed using FullProf Suite software. $K_2Ho(PO_4)(WO_4)$ was used as a reference (PDF4+ (ICDD) 04-015-9304) [28]. The refinement results for KGPW, KGPW:20%Tb^{3+}, KGPW:20%Eu^{3+}, and KGPW:10%Yb^{3+},20%Tb^{3+},20%Eu^{3+} samples are shown in Figure 2. The obtained unit cell parameters are given in Table S5. As anticipated, the lattice parameters decreased if samples were doped with Yb^{3+} and Eu^{3+} due to the smaller ionic radii when compared to Gd^{3+}.

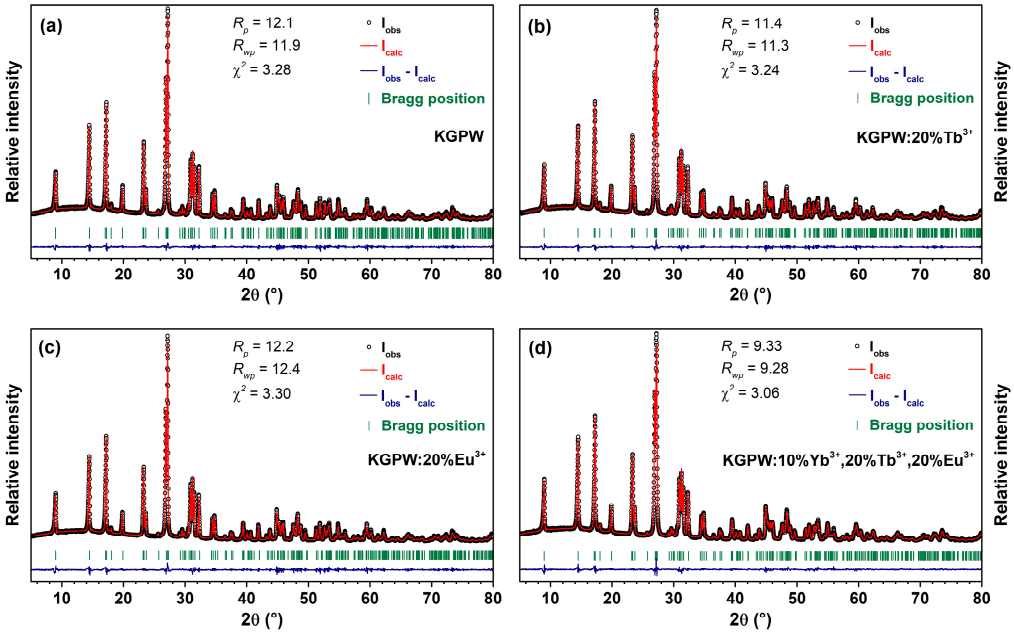

Figure 2. Rietveld refinement data for undoped KGPW (**a**), KGPW:20%Tb^{3+} (**b**), KGPW:20%Eu^{3+} (**c**), and KGPW:10%Yb^{3+}, 20%Tb^{3+}, 20%Eu^{3+} (**d**).

The morphological features of KGPW powders doped with Yb^{3+}, Tb^{3+}, and Eu^{3+} were evaluated by taking SEM images, which are shown in Figures S3 and S4 under different magnifications. The powder particles consist of irregularly shaped small crystallites which are heavily agglomerated. No significant difference in crystallite shape and size was observed between the samples doped with different concentrations of lanthanide ions.

3.2. Photoluminescence Studies

The reflection spectra of KGPW:10%Yb^{3+} (black line), KGPW:20%Tb^{3+} (green line), and KGPW:20%Eu^{3+} (red line) samples are given in Figure 3a–c, respectively. The reflection spectra were measured in the range from 250 to 800 nm. The sample doped with Eu^{3+} possesses typical Eu^{3+} absorption lines originating from the $^7F_0$ and $^7F_1$ energy levels. The observed Eu^{3+} absorption lines are assigned to $^7F_0 \rightarrow {}^5H_J$ (ca. 318 nm), $^7F_0 \rightarrow {}^5D_4$ (ca. 360 nm), $^7F_0 \rightarrow {}^5L_{7,8}$; ^5G_J (ca. 374–390 nm), $^7F_0 \rightarrow {}^5L_6$ (ca. 390–402 nm), $^7F_0 \rightarrow {}^5D_3$ (ca. 418 nm), $^7F_0 \rightarrow {}^5D_2$ (ca. 465 nm), $^7F_0 \rightarrow {}^5D_1$ (ca. 526 nm), $^7F_1 \rightarrow {}^5D_1$ (ca. 530–539 nm), and $^7F_1 \rightarrow {}^5D_0$ (ca. 594 nm). The sample doped with Tb^{3+} shows two sets of absorption

lines, which are attributed to the Tb^{3+} $^7F_6 \rightarrow {}^5L_9$ (ca. 346–361 nm) and $^7F_6 \rightarrow {}^5L_{10}$; $^5D_3$ (ca. 361–384 nm) transitions [29]. The body color of the sample doped with Tb^{3+} was brownish; therefore, the reflectance values at longer wavelengths were lower when compared to the sample containing no Tb^{3+}. The brownish color is likely caused by traces of Tb^{4+} present in the samples due to the incomplete reduction in terbium to the trivalent state. In this case, the charge transfer between Tb^{3+} and Tb^{4+} occurs after absorption of photons in the entire visible range (Tb_4O_7 ($Tb_2O_3 \cdot 2TbO_2$), used in synthesis, for instance, is dark brown). The broad absorption band observed in all three samples in the range of 250–340 nm could be attributed to the host lattice absorption. The reflection spectra of co-doped samples are depicted in Figure S5. All the co-doped samples show typical sets of absorption lines of the dopant ions. The reflectance values at longer wavelengths decrease to 90–95% if the samples are co-doped with Tb^{3+}. The absorption lines are the same as in the singly doped samples and are attributed to Eu^{3+} or Tb^{3+} ions.

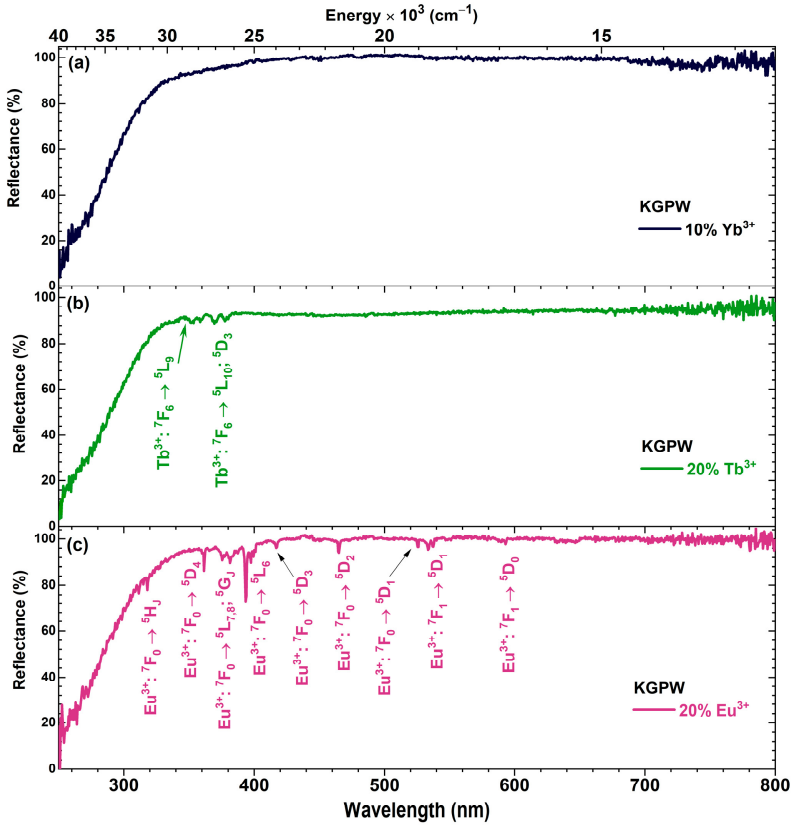

Figure 3. Reflection spectra of (**a**) KGPW:10%Yb^{3+} (black line), (**b**) KGPW:20%Tb^{3+} (green line), and (**c**) KGPW:20%Eu^{3+} (red line).

The reflection spectrum of undoped KGPW was used to determine the bandgap of the host material. Firstly, the reflection spectrum was converted to a Tauc plot. The subsequent linear approximation of the obtained spectrum showed that the bandgap of KGPW was 3.8 eV.

The excitation (λ_{em} = 614 nm) spectra of undoped KGPW, KGPW:20%Tb^{3+}, KGPW:20%Eu^{3+}, and KGPW:20%Tb^{3+},20%Eu^{3+} are depicted in Figure 4. The excitation spectrum (please refer to Figure 4a) of the undoped KGPW host matrix contains three sets of Gd^{3+} excitation lines: $^8S \rightarrow {}^6I_J$ (ca. 270–279 nm), $^8S \rightarrow {}^6P_{5/2}$ (ca. 305 nm), and $^8S \rightarrow {}^6P_{7/2}$ (ca. 311 nm) [30]. Since Gd^{3+} ions do not emit at 614 nm, there should be no excitation lines at all; therefore, it is likely that this sample contains traces of Eu^{3+} coming either from transport reactions in the furnace or impurities in the starting materials. This assumption is supported by a weak excitation line at ca. 394 nm, which is typical for the $^7F_0 \rightarrow {}^5L_6$

transition of Eu^{3+}. The same weak excitation line was also observed for the KGPW:10%Yb^{3+} sample (please refer to Figure S6b). The excitation spectrum of the KGPW:20%Tb^{3+} (please refer to Figure 4b) sample possesses typical Tb^{3+} excitation lines originating from $^7F_6$ ground state level transitions to $^5H_7$ (ca. 316–323 nm), $^5D_1$ (ca. 324–332 nm), $^5L_{7;8}$ (ca. 335–346 nm), $^5D_2$; $^5L_9$ (ca. 347–356 nm), $^5G_5$ (ca. 359 nm), $^5L_{10}$ (ca. 365–373 nm), $^5D_3$; $^5G_6$ (ca. 375–384 nm), and $^5D_4$ (ca. 486 nm) excited state levels [29]. The excitation spectrum of the KGPW:20%Eu^{3+} (please refer to Figure 4c) sample possesses the same sets of excitation lines, which were also detected in the reflection spectrum. The excitation spectrum of the KGPW:20%Tb^{3+},20%Eu^{3+} sample shows transitions of all three ions (Gd^{3+}, Tb^{3+}, and Eu^{3+}) (please refer to Figure 4d). As predicted, the most intense transition line is attributed to Eu^{3+} $^7F_0 \rightarrow {}^5L_6$ (ca. 394 nm) because emission was monitored at a 614 nm wavelength. Excitation spectra of KGPW:10%Yb^{3+},20%Tb^{3+},20%Eu^{3+} and KGPW:10%Yb^{3+} (λ_{em} = 614 nm) are depicted in Figure S6a and Figure S6b, respectively. The excitation spectra of the KGPW:10%Yb^{3+} sample also showed three typical Gd^{3+} excitation lines as well as a vanishingly small Eu^{3+} excitation line at ca. 394 nm, indicating that a small amount of Eu^{3+} ions is present in the sample.

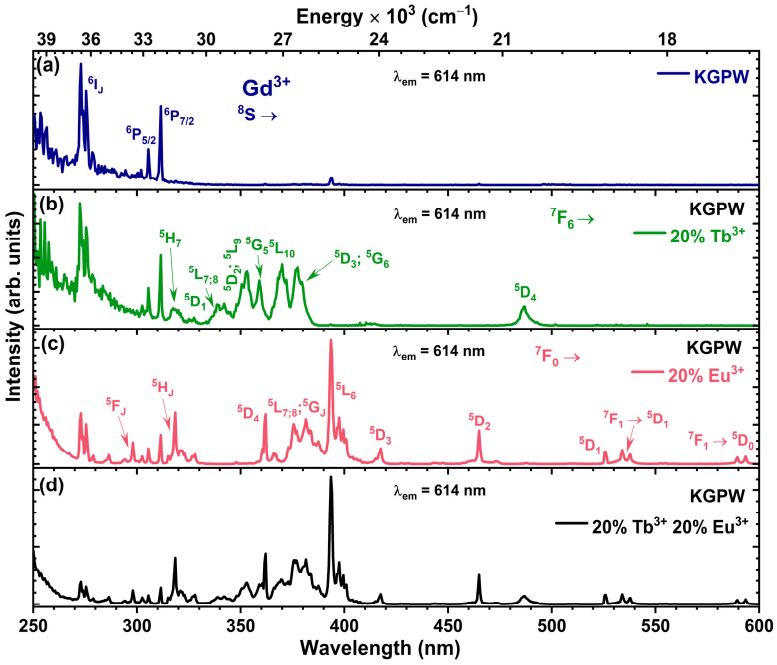

Figure 4. Excitation (λ_{em} = 614 nm) spectra of (**a**) undoped KGPW, (**b**) KGPW:20%Tb^{3+}, (**c**) KGPW:20%Eu^{3+}, and (**d**) KGPW:20%Tb^{3+},20%Eu^{3+}.

The emission spectra (λ_{ex} = 340 nm) of KGPW:20%Tb^{3+},Eu^{3+} and KGPW:10%Yb^{3+},20%Tb^{3+},Eu^{3+} doped with 0% and 20% of Eu^{3+} are depicted in Figure 5 and Figure S7, respectively. Since Yb^{3+} cannot be excited with 340 nm wavelength radiation, the introduction of Yb^{3+} into the crystal lattice has no significant effect on the emission spectra of Tb^{3+} and Eu^{3+}. The KGPW:20%Tb^{3+} sample shows typical Tb^{3+} emission lines originating from $^5D_4 \rightarrow {}^7F_6$ (ca. 480–500 nm), $^5D_4 \rightarrow {}^7F_5$ (ca. 535–560 nm), $^5D_4 \rightarrow {}^7F_4$ (ca. 577–592 nm), and $^5D_4 \rightarrow {}^7F_3$ (ca. 613–627 nm) optical transitions. No emission lines that could be attributed to Eu^{3+} were observed in solely Tb^{3+}-doped samples. Completely different spectra were observed when Eu^{3+} ions were included in the samples. The Eu^{3+}-concentration-dependent emission spectra of KGPW:20%Tb^{3+} under 340 nm excitation are shown in Figure S8. The integrated intensity of the samples increases with increasing Eu^{3+}, although the intensity of Tb^{3+} transitions such as $^5D_4 \rightarrow {}^7F_6$ and $^5D_4 \rightarrow {}^7F_5$ drastically decrease with increasing Eu^{3+} concentration. Thus, as it was expected, the emission intensity of the Eu^{3+} $^5D_0 \rightarrow {}^7F_2$ transition coherently increases with increasing Eu^{3+} concentration and reaches the highest intensity in the 20%Eu^{3+}-doped sample. A similar tendency was observed

with KGPW:10%Yb^{3+},20%Tb^{3+},Eu^{3+} as a function of Eu^{3+} concentration (please refer to Figure S9). However, contrary to the tendency discussed earlier, the integrated intensity of samples increases up to 5% Eu^{3+} and then slightly decreases. As we can see from the emission spectra (λ_{ex} = 340 nm), the energy from Tb^{3+} is transferred to Eu^{3+}; therefore, we see the emission lines attributed to both Tb^{3+} and Eu^{3+} optical transitions. Emission spectra of the samples doped with Eu^{3+} and Tb^{3+} show typical Eu^{3+} emission lines, whereas the Tb^{3+} emission intensity drastically decreases with increasing Eu^{3+} concentration in the material and almost vanishes when Eu^{3+} concentration reaches 20%. Both samples, KGPW:20%Tb^{3+},20%Eu^{3+} and KGPW:10%Yb^{3+},20%Tb^{3+},20%Eu^{3+}, show typical Eu^{3+} emission lines in the ranges 583–600 nm ($^5D_0 \rightarrow {}^7F_1$), 605–630 nm ($^5D_0 \rightarrow {}^7F_2$), 645–655 nm ($^5D_0 \rightarrow {}^7F_3$), and 688–708 nm ($^5D_0 \rightarrow {}^7F_4$) [31].

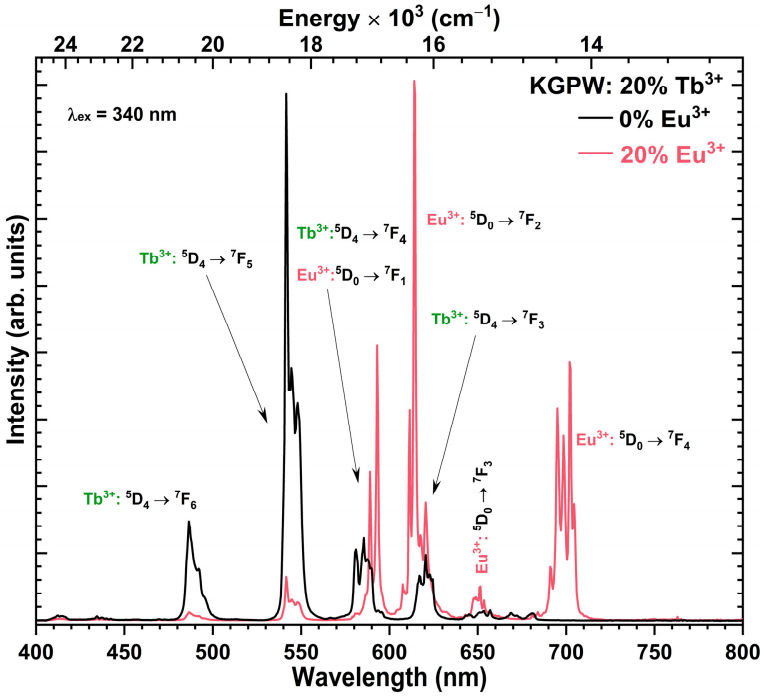

Figure 5. Emission (λ_{ex} = 340 nm) spectra of KGPW:20%Tb^{3+},Eu^{3+} as a function of Eu^{3+} concentration.

The Eu^{3+} concentration-dependent UC emission spectra of KGPW:10%Yb^{3+},20%Tb^{3+},Eu^{3+} samples were measured under 980 nm wavelength laser excitation. The UC emission spectra of 1% and 20% Eu^{3+}-doped specimens are depicted in Figure 6. The inset graph shows normalized integrated emission intensity as a function of Eu^{3+} concentration. The overall UC emission intensity of the samples increases until Eu^{3+} concentration reaches 10%. Increasing the Eu^{3+} concentration further resulted in a decrease in overall UC emission which is likely caused by concentration quenching due to increased probability of cross-relaxation between adjacent Eu^{3+} [32]. Both UC emission spectra of KGPW:10%Yb^{3+},20%Tb^{3+} doped with 1% and 20% Eu^{3+} show typical Tb^{3+} and Eu^{3+} emission lines. The most intense emission line in the sample doped with 20% Tb^{3+} and 1% Eu^{3+} ions is attributed to Tb^{3+} $^5D_4 \rightarrow {}^7F_5$ (λ = 542 nm); for the sample doped with 20% Tb^{3+} and 20% Eu^{3+}, as predicted, the most intense emission line is attributed to Eu^{3+} $^5D_0 \rightarrow {}^7F_2$ (λ = 614 nm).

The normalized UC emission spectra (λ_{ex} = 980 nm) of KGPW:10%Yb^{3+},20%Tb^{3+}, KGPW:10%Yb^{3+},20%Tb^{3+},2.5%Eu^{3+}, and KGPW:10%Yb^{3+},20%Tb^{3+},20%Eu^{3+} are shown in Figure S10. The spectra were normalized to the most intense Tb^{3+} transition ($^5D_4 \rightarrow {}^7F_5$ ca. 541.5 nm) in order to better evaluate the change between Tb^{3+} and Eu^{3+} emission intensity upon increasing Eu^{3+} concentration. It is evident that Eu^{3+} emission intensity increases with increasing Eu^{3+} concentration. This indicates that $Tb^{3+} \rightarrow Eu^{3+}$ energy transfer becomes more efficient at higher Eu^{3+} concentrations.

For a further understanding of down-shifting emission, the photoluminescence (PL) decay curves were recorded and analyzed. Samples were excited with 340 nm radiation ($^7F_6 \rightarrow {}^5L_{7;8}$ transitions of Tb^{3+}), and the emission was monitored at 542 nm ($^5D_4 \rightarrow {}^7F_5$ transition of Tb^{3+}) and 614 nm ($^5D_4 \rightarrow {}^7F_3$ transition of Tb^{3+} and $^5D_0 \rightarrow {}^7F_2$ transition of Eu^{3+}) (please refer to Figure 7). The effective PL lifetime values were calculated using the following equation [33]:

$$\tau_{eff} = \frac{\int_0^\infty I(t)t\,dt}{\int_0^\infty I(t)\,dt} \quad (1)$$

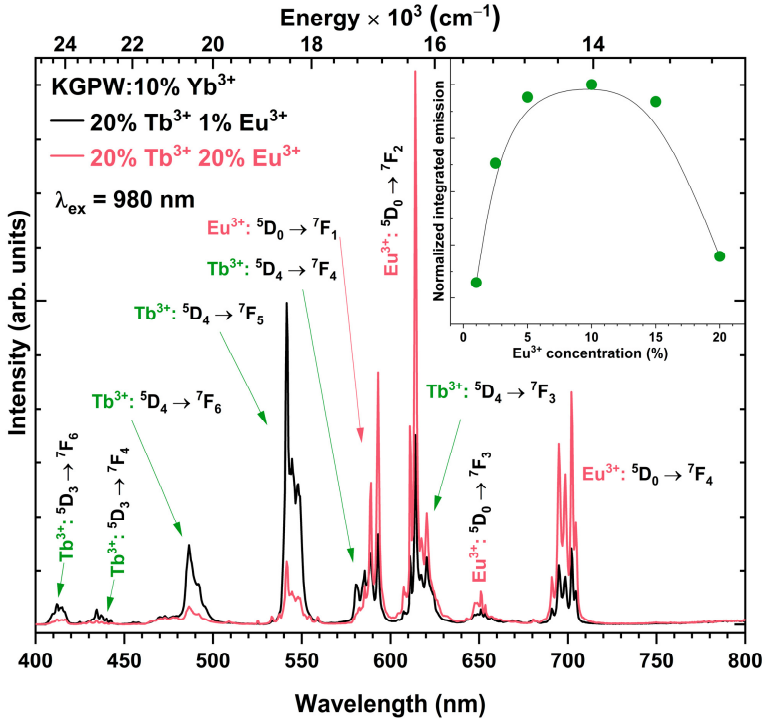

Figure 6. UC emission spectra of KGPW:10%Yb^{3+},20%Tb^{3+},Eu^{3+} as a function of Eu^{3+} concentration under 980 nm laser excitation. The inset shows normalized integrated UC emission intensity as a function of Eu^{3+} concentration.

Here, *I(t)* is PL intensity at a given time *t*. The PL decay curves of all synthesized samples as a function of Eu^{3+} concentration are shown in Figure 7. Figure 7a,b show the PL decay curves (λ_{ex} = 340 nm; λ_{em} = 542 nm) of KGPW:20%Tb^{3+},Eu^{3+} and KGPW:10%Yb^{3+},20%Tb^{3+},Eu^{3+} specimens as a function of Eu^{3+} concentration. With increasing Eu^{3+} concentration, the PL decay curves become steeper, suggesting that PL lifetime values decrease. The calculated effective PL lifetime values for the given samples are presented in Figure 7c. The effective PL lifetime values for KGPW:20%Tb^{3+},Eu^{3+} samples decrease from 2286 ± 2 µs to 1486 ± 7 µs if Eu^{3+} concentration increases from 0% to 20%. A similar trend was also observed for the KGPW:10%Yb^{3+},20%Tb^{3+},Eu^{3+} samples where the effective PL lifetime values decreased from 2236 ± 2 µs to 1565 ± 6 µs with increasing Eu^{3+} concentration from 0% to 20%, respectively. The effective PL lifetime values for the samples doped with other Eu^{3+} concentrations are tabulated in Table S6. Figure 7d,e show the PL decay curves (λ_{ex} = 340 nm, λ_{em} = 614 nm) of KGPW:20%Tb^{3+},Eu^{3+} and KGPW:10%Yb^{3+},20%Tb^{3+},Eu^{3+} samples as a function of Eu^{3+} concentration, respectively. The PL decay curves become steeper with increasing Eu^{3+} concentration. The calculated effective PL lifetime values slightly decrease from 2712 ± 3 µs to 2511 ± 2 µs for KGPW:20%Tb^{3+},Eu^{3+} samples with increasing Eu^{3+} concentration from 1% to 20%. The effective PL lifetime values of KGPW:10%Yb^{3+},20%Tb^{3+},Eu^{3+} samples, in turn, decrease from 2550 ± 3 µs to 2085 ± 4 µs for 1% and 20% Eu^{3+}-doped specimens, respectively.

The trend of effective PL lifetime values decreasing with increasing Eu^{3+} concentration is depicted in Figure 7f, and the exact calculated PL lifetime values are tabulated in Table S7.

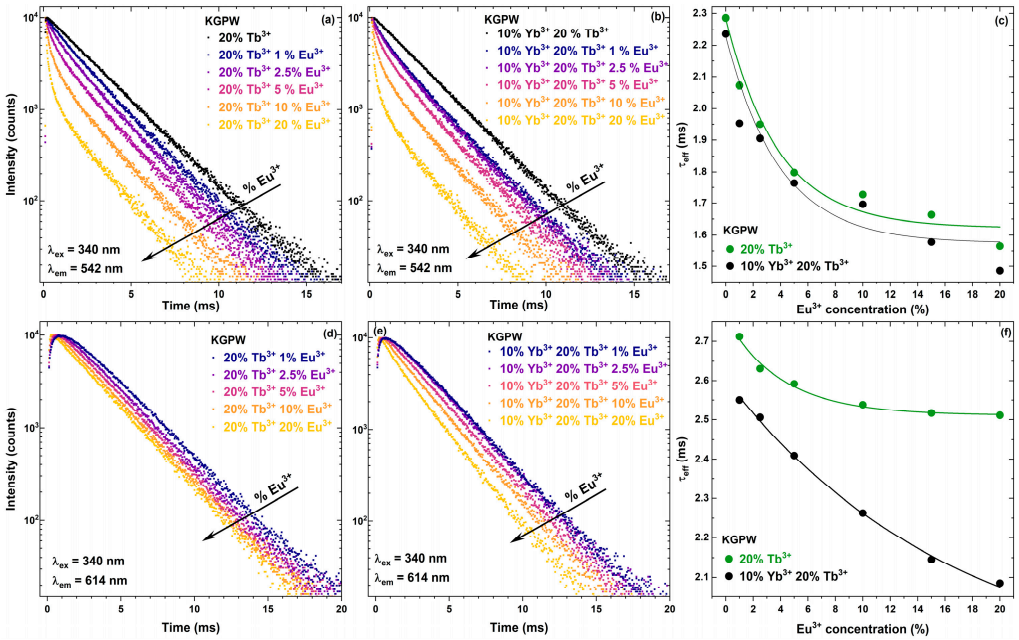

Figure 7. PL decay curves of KGPW:20%Tb^{3+},Eu^{3+} (**a**) and KGPW:10%Yb^{3+},20%Tb^{3+},Eu^{3+} (**b**), and PL lifetime values (**c**) as a function of Eu^{3+} concentration (λ_{ex} = 340 nm, λ_{em} = 542 nm). PL decay curves of KGPW:20%Tb^{3+},Eu^{3+} (**d**) and KGPW:10%Yb^{3+},20%Tb^{3+},Eu^{3+} (**e**), and PL lifetime values (**f**) as a function of Eu^{3+} concentration (λ_{ex} = 340 nm, λ_{em} = 614 nm).

In order to understand the UC process of the prepared materials, the PL decay curves under 980 nm laser excitation were measured, monitoring emission at 542 nm (Tb^{3+}), 704 nm (Eu^{3+}), and 1050 nm (Yb^{3+}). The effective UC PL lifetime and rise time values were calculated and tabulated in Tables S8–S10. The UC PL decay curves of the KGPW:10%Yb^{3+},20%Tb^{3+},Eu^{3+} samples as a function of Eu^{3+} concentration for the Tb^{3+} $^5D_4$ $\rightarrow$ $^7F_5$ (λ_{em} = 542 nm) transition are depicted in Figure 8a. It is evident that the UC PL decay curves of Tb^{3+} become steeper with increasing Eu^{3+} concentration. Figure 8b,c show the UC PL rise time and UC PL lifetime values of the same samples as a function of Eu^{3+} concentration. Both figures indicate that the UC PL rise time and UC PL lifetime values decrease with increasing Eu^{3+} concentration. The UC PL rise time values decrease from 284 $\pm$ 7 µs to 113 $\pm$ 10 µs if Eu^{3+} concentration increases from 0% to 20%, whereas the UC PL lifetime values decrease from 2055 $\pm$3 µs to 1345 $\pm$15 µs, respectively. The decreasing Tb^{3+} UC PL lifetime values show that Tb^{3+} $\rightarrow$ Eu^{3+} energy transfer efficiency increases with increasing Eu^{3+} concentration.

Decay curves of Eu^{3+} $^5D_0$ $\rightarrow$ $^7F_4$ transition (λ_{ex} = 980 nm, λ_{em} = 704 nm) for the KGPW:10%Yb^{3+}20%Tb^{3+} sample as a function of Eu^{3+} concentration were recorded and depicted in Figure 9a. The calculated PL rise time and lifetime values of the samples are shown in Figures 9b and 9c, respectively. The UC PL decay curves become steeper with increasing Eu^{3+} concentration due to the increasing probability of cross-relaxation processes between Eu^{3+} ions. Thus, the PL rise time and lifetime values decrease in samples with higher Eu^{3+} concentration. The UC PL rise time values decrease from 780 $\pm$80 µs to 334 $\pm$18 µs, whereas the UC PL lifetime values decrease from 2414 $\pm$ 3 µs to 1765 $\pm$ 3 µs.

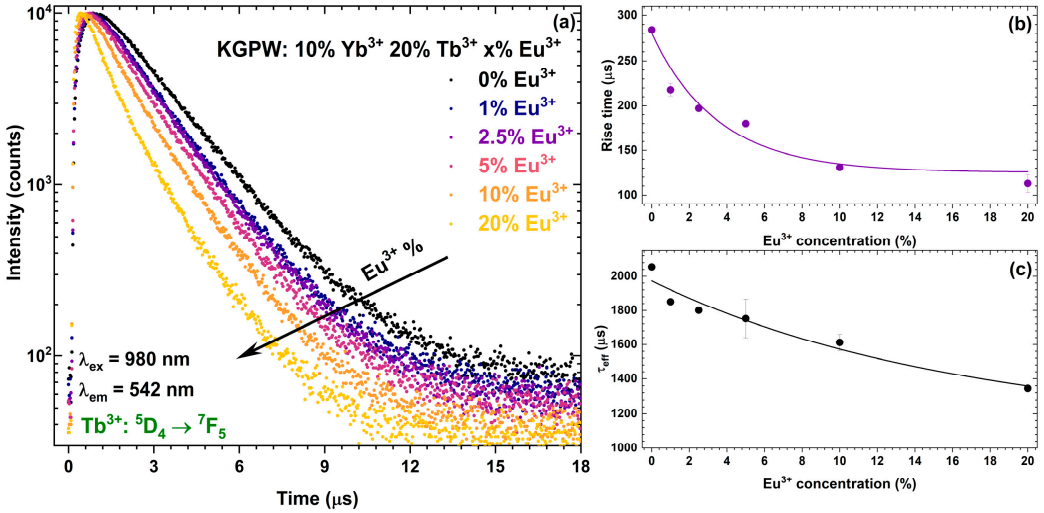

Figure 8. Eu^{3+} concentration-dependent UC PL decay curves (λ_{ex} = 980 nm, λ_{em} = 542 nm) (**a**), UC PL rise time (**b**), and UC PL lifetime values (**c**) of KGPW:10%Yb^{3+},20%Tb^{3+},Eu^{3+} samples.

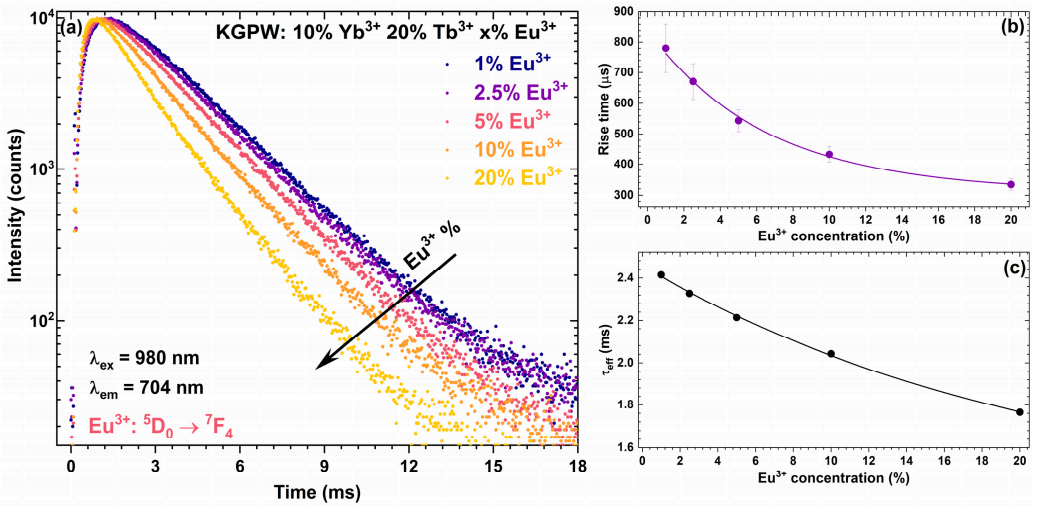

Figure 9. Eu^{3+} concentration-dependent UC PL decay curves (λ_{ex} = 980 nm, λ_{em} = 704 nm) (**a**), UC PL rise time (**b**), and UC PL lifetime values (**c**) of KGPW:10%Yb^{3+},20%Tb^{3+},Eu^{3+} samples.

The $Tb^{3+} \rightarrow Eu^{3+}$ energy transfer efficiency (η_{tr}) can be estimated using the given equation [34]:

$$\eta_{tr} = 1 - \frac{\tau_S}{\tau_{S0}} \quad (2)$$

Here, τ_S and τ_{S0} are PL lifetime values of Tb^{3+} in the presence and absence of Eu^{3+}, respectively. The calculated energy transfer efficiency values as a function of Eu^{3+} concentration are depicted in Figure S11. The η_{tr} values gradually increase with increasing Eu^{3+} concentration. For instance, η_{tr} values increase from 10.0% to 34.6% if Eu^{3+} concentration increases from 1% to 20% in the KGPW:10%Yb^{3+},20%Tb^{3+},Eu^{3+} samples (λ_{ex} = 980 nm, λ_{em} = 542 nm). A similar tendency was also observed for KGPW:20%Tb^{3+},Eu^{3+} and KGPW:10%Yb^{3+},20%Tb^{3+},Eu^{3+} samples (λ_{ex} = 340 nm, λ_{em} = 542 nm) where η_{tr} values increase from 9.4% to 31.5% and from 12.7% to 33.5%, respectively.

To evaluate the PL lifetime values of Yb^{3+}, the PL decay curves (λ_{ex} = 980 nm, λ_{em} = 1050 nm) for Yb^{3+} $^2F_{5/2} \rightarrow {}^2F_{7/2}$ transition were recorded (please refer to Figure S12). The PL decay curves become slightly steeper with increasing Eu^{3+} concentration, although PL lifetime values of the samples are almost the same: 1048 ± 2 μs for the sample with 0% Eu^{3+} and 924 ± 1 μs for the sample with 20% Eu^{3+}. Whereas the PL lifetime of the

KGPW:10%Yb^{3+} sample is 1066 ± 2 µs. This feature indicates that the percentage of Eu^{3+} doping has an insignificant impact on PL lifetime values of Yb^{3+} ions.

The UC PL decay curves (λ_{ex} = 980 nm, λ_{em} = 542 nm) and UC emission spectra (λ_{ex} = 980 nm) of the KGPW:10%Yb^{3+},20%Tb^{3+},5%Eu^{3+} sample as a function of temperature are shown in Figure 10. It is interesting to note that the overall UC emission intensity increases with increasing temperature up to 200 K. The UC emission intensity decreases if the temperature is increased further. It was also observed that the PL decay curves of the same sample change insignificantly with increasing temperature indicating that Tb^{3+} PL lifetime values are relatively stable within a 77–350 K temperature range. Such observation indicates that $Tb^{3+} \rightarrow Eu^{3+}$ energy transfer does not change in the same temperature range (i.e., 77 to 350 K). Moreover, the intensity ratio between Tb^{3+} $^5D_4 \rightarrow {}^7F_5$ (ca. 550 nm) and Eu^{3+} $^5D_0 \rightarrow {}^7F_2$ (ca. 620 nm) transitions is virtually the same regardless of the temperature.

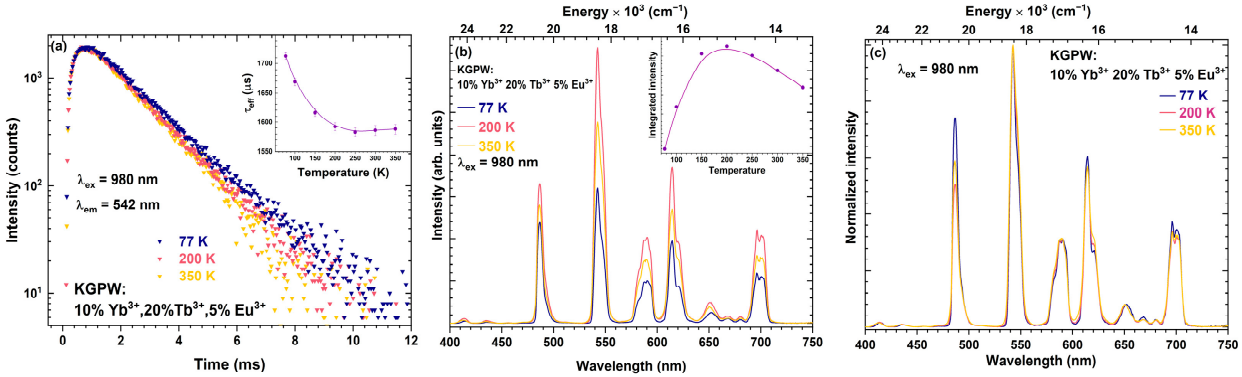

Figure 10. Temperature-dependent UC PL decay and emission spectra of KGPW:10%Yb^{3+},20%Tb^{3+},5%Eu^{3+} sample: (**a**) UC PL decay curves (λ_{ex} = 980 nm, λ_{em} = 542 nm), (**b**) UC emission spectra (λ_{ex} = 980 nm) (inset shows integrated emission intensity), (**c**) normalized emission spectra.

3.3. Photometric

In order to demonstrate the emission color dependency of the Eu^{3+} concentration of the synthesized phosphors, the chromaticity coordinates in 1931 color space diagrams were calculated and depicted in Figure 11. The color coordinates of the KGPW:10%Yb^{3+},20%Tb^{3+},Eu^{3+} shifted linearly from the green area (sample with 0% Eu^{3+}) to the red area (sample with 20% Eu^{3+}). The color coordinates of the synthesized samples indicate that the emission color of the sample could be varied by changing the Eu^{3+} concentration. This was also confirmed by taking digital images of the phosphors in daylight and under 365 nm excitation (please refer to Figure S13). The temperature-dependent color coordinates of KGPW:10%Yb^{3+},20%Tb^{3+},5%Eu^{3+} are located in the green area and do not shift to the red area when raising the temperature from 77 to 500 K. The exact calculated Eu^{3+} and temperature-dependent color coordinates are summarized in Tables S11 and S12, n.

3.4. Quantum Yield

In order to evaluate the possible practical value of the synthesized compounds, the external quantum efficiency was calculated. The obtained external quantum efficiencies of KGPW:20%Tb^{3+},Eu^{3+} and KGPW:10%Yb^{3+},20%Tb^{3+},Eu^{3+} samples upon 340 nm excitation are given in Figure S14. The external quantum efficiency was calculated using this formula [35]:

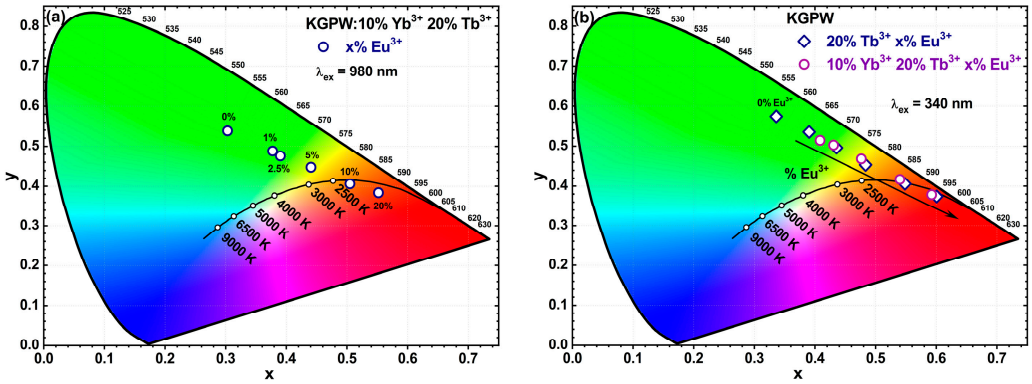

Figure 11. CIE 1931 color space diagrams with color coordinates of (**a**) KGPW:10%Yb^{3+},20%Tb^{3+},Eu^{3+} (λ_{ex} = 980 nm), and (**b**) KGPW doped with 20% Tb^{3+} and co-doped with 10%Yb^{3+} and 20%Tb^{3+} as a function of Eu^{3+} concentration (λ_{ex} = 340 nm).

$$QE = \frac{\int I_{em,\ sample} - \int I_{em,\ BaSO_4}}{\int I_{ref,\ BaSO_4} - \int I_{ref,\ sample}} \times 100\% = \frac{N_{em}}{N_{abs}} \times 100\% \quad (3)$$

Here, $\int I_{em,\ sample}$ and $\int I_{em,\ BaSO_4}$ are integrated emission intensities of the phosphor sample and $BaSO_4$, respectively. $\int I_{ref,\ sample}$ and $\int I_{ref,\ BaSO_4}$ are the integrated reflectance of the phosphor sample and $BaSO_4$, respectively. N_{em} is the number of emitted photons and N_{abs} is the absorbed photons. A further increase in Eu^{3+} concentration shows a slight decrease in quantum efficiency in KGPW:20%Tb^{3+} samples (the *QE* varies in the 10–13.5% range). The highest *QE* value was 13.75% and was obtained for the KGPW:20%Tb^{3+},1%Eu^{3+} sample. However, the KGPW:10%Yb^{3+},20%Tb^{3+},Eu^{3+} samples show lower *QE* values compared to their KGPW:20%Tb^{3+},Eu^{3+} counterparts. The *QE* values vary from 5% to 9%, and the highest quantum efficiency of 9.21% was achieved with the KGPW:10%Yb^{3+},20%Tb^{3+},2.5%Eu^{3+} sample. The relatively low *QE* could be explained due to cross-relaxation processes in the samples.

4. Conclusions

All in all, we have successfully prepared phase-pure KGPW:20%Tb^{3+},Eu^{3+} and KGPW:10%Yb^{3+},20%Tb^{3+},Eu^{3+} where Eu^{3+} concentrations varied from 1% to 20% Eu^{3+}. All the prepared samples, depending on the Tb^{3+}/Eu^{3+} concentration ratio, emit in a green-to-red spectral range under 340 and 980 nm excitation. Emission spectra of the samples doped with Eu^{3+} and Tb^{3+} under 340 nm excitation show typical Eu^{3+} and Tb^{3+} emission lines, whereas the Tb^{3+} emission intensity drastically decreases with increasing Eu^{3+} concentration. The strongest down conversion emission intensity was obtained for KGPW:20%Tb^{3+},20%Eu^{3+} and KGPW:10%Yb^{3+},20%Tb^{3+},5%Eu^{3+} samples. The UC emission spectra of the KGPW:10%Yb^{3+},20%Tb^{3+},5%Eu^{3+} sample under 980 nm excitation showed an interesting feature, namely, that the overall UC emission intensity increases when increasing the temperature up to 200 K and then slightly decreases. The strongest up-conversion emission in the visible range was achieved with KGPW:10%Yb^{3+},20%Tb^{3+},10%Eu^{3+} under 980 nm excitation. The color coordinates of the phosphor samples can be varied from a green-to-red spectral range by adjusting the Eu/Tb ratio.

Supplementary Materials: The following supporting information can be downloaded at: https://www.mdpi.com/article/10.3390/cryst13030479/s1, Table S1. Spectrometer settings for measuring reflection spectra of KGPW:20%Tb^{3+},Eu^{3+} and KGPW:10%Yb^{3+},20%Tb^{3+},Eu^{3+} phosphors. Table S2. Spectrometer settings for measuring excitation spectra of KGPW:10% Yb^{3+} 20% Tb^{3+} x% Eu^{3+} phosphors. Table S3. Spectrometer settings for measuring down-shifting emission spectra of KGPW:20%Tb^{3+}, Eu^{3+} and KGPW:10%Yb^{3+},20%Tb^{3+}, Eu^{3+} phosphors. Table S4. Spectrometer settings for measuring UC emission spectra of KGPW:10%Yb^{3+},20%Tb^{3+}, Eu^{3+} phosphors. Table S5. Lattice parameters of KGPW, KGPW:10%Yb^{3+}, KGPW:20%Tb^{3+}, KGPW:20%Eu^{3+}, and

KGPW:10%Yb^{3+}20%Tb^{3+}20%Eu^{3+} samples derived from Rietveld refinement analysis. Table S6. The calculated effective PL lifetime values of KGPW:20%Tb^{3+}, Eu^{3+} and KGPW:10%Yb^{3+},20%Tb^{3+},Eu^{3+} phosphors as a function of Eu^{3+} concentration (λ_{ex} = 340 nm, λ_{em} = 542 nm). Table S7. The calculated effective PL lifetime values of KGPW:20%Tb^{3+}, Eu^{3+} and KGPW:10%Yb^{3+},20%Tb^{3+}, Eu^{3+} phosphors as a function of Eu^{3+} concentration (λ_{ex} = 340 nm, λ_{em} = 614 nm). Table S8. The UC PL rise time and UC PL lifetime values of Tb^{3+} in KGPW:10%Yb^{3+},20%Tb^{3+}, Eu^{3+} phosphors as a function of Eu3+ concentration (λ_{ex} = 980 nm, λ_{em} = 542 nm). Table S9. The UC PL rise time and UC PL lifetime values of Eu^{3+} in KGPW:10%Yb^{3+},20%Tb^{3+}, Eu^{3+} phosphors as a function of Eu^{3+} concentration (λ_{ex} = 980 nm, λ_{em} = 614 nm). Table S10. The PL lifetime values of Yb^{3+} in KGPW (λ_{ex} = 980 nm, λ_{em} = 1050 nm). Table S11. Color coordinates (CIE 1931 color space) of the synthesized phosphors as a function of Eu^{3+} concentration under 340 nm and 980 nm excitation. Table S12. Color coordinates (CIE 1931 color space) of KGPW:10%Yb^{3+},20%Tb^{3+},5%Eu^{3+} sample as a function of temperature (λ_{ex} = 980 nm). Figure S1. Emission spectra of KGPW:10%Yb^{3+},20%Tb^{3+},20%Eu^{3+} and KGPW:10%Yb^{3+},20%Eu^{3+} under 980 nm laser excitation. Figure S2. XRD patterns of KGPW doped with 20% Tb^{3+} (a), 20% Eu^{3+} (b), 10% Yb^{3+} (c), co-doped with 10% Yb^{3+} and 20% Tb^{3+} (d), 20% Tb^{3+} and 20% Eu^{3+} (e), and 10% Yb^{3+}, 20% Tb^{3+}, 20% Eu^{3+} (f). The reference pattern of $K_2Bi(PO_4)(WO_4)$ is given for comparison (PDF4+ 04-013-4256). Figure S3. SEM images of KGPW:20%Tb^{3+},20%Eu^{3+} (a) and (d), KGPW:10%Yb^{3+},20%Eu^{3+} (b) and (e), and KGPW:10%Yb^{3+},20% Tb^{3+},20%Eu^{3+} (c) and (f) under different magnification. Figure S4. SEM images of KGPW:10%Yb^{3+} (a) and (d), KGPW:20%Tb^{3+} (b) and (e), and KGPW:20%Eu^{3+} (c) and (f). Figure S5. Reflection spectra of KGPW:20%Tb^{3+},20%Eu^{3+} (black line), KGPW:10%Yb^{3+},20%Tb^{3+},20%Eu^{3+} (blue line), and KGPW:20%Eu^{3+} (red line) (a). KGPW:10%Yb^{3+},20%Tb^{3+} (black line), KGPW:20%Tb^{3+} (red line), and KGPW:10%Yb^{3+} (blue line) (b). Figure S6. Excitation spectra (λ_{em} = 614 nm) of KGPW doped with (a) 10%Yb^{3+},20% Tb^{3+},20%Eu^{3+}, and (b) doped with 10% Yb^{3+}. Figure S7. Emission (λ_{ex} = 340 nm) spectra of KGPW:10%Yb^{3+},20%Tb^{3+},Eu^{3+} as a function of Eu^{3+} concentration. Figure S8. Emission spectra of KGPW:20%Tb^{3+}, Eu^{3+} as a function of Eu^{3+} concentration (λ_{ex} = 340 nm). The inset graph shows integrated emission intensity as a function of Eu^{3+} concentration. Figure S9. Emission spectra of KGPW:10%Yb^{3+},20%Tb^{3+}, Eu^{3+} as a function of Eu^{3+} concentration (λ_{ex} = 340 nm). The inset graph shows integrated emission intensity as a function of Eu^{3+} concentration. Figure S10. UC emission spectra (normalized to 541.5 nm) of KGPW:10%Yb^{3+},20%Tb^{3+}, KGPW:10%Yb^{3+},20%Tb^{3+},2.5%Eu^{3+}, and KGPW:10%Yb^{3+},20%Tb^{3+},20%Eu^{3+} (λ_{ex} = 980 nm). Figure S11. $Tb^{3+} \rightarrow Eu^{3+}$ energy transfer efficiency as a function of Eu^{3+} concentration. Figure S12. Yb^{3+} PL decay curves (λ_{ex} = 980 nm, λ_{em} = 1050 nm) in KGPW:10%Yb^{3+} and KGPW:10%Yb^{3+},20%Tb^{3+} samples as a function of Eu^{3+} concentration. Figure S13. Digital images of the synthesized samples in daylight (a) and under 365 nm excitation (b). Figure S14. The external quantum efficiency of all synthesized samples as a function of Eu^{3+} concentration (λ_{ex} = 340 nm).

Author Contributions: Conceptualization, A.K.; investigation, J.G.; writing—original draft preparation, J.G.; writing—review and editing, A.K.; visualization J.G. and A.K.; funding acquisition, A.K. All authors have read and agreed to the published version of the manuscript.

Funding: This research was funded by a grant (No. D-2018-0703 "Controlling the up-conversion emission by tuning band gap of the host matrix") from the Research Council of Lithuania.

Institutional Review Board Statement: Not applicable.

Informed Consent Statement: Not applicable.

Data Availability Statement: The data presented in this study are available on request from the corresponding author.

Acknowledgments: The authors gratefully thank Andrius Pakalniskis (Vilnius University) for taking SEM images.

Conflicts of Interest: The authors declare no conflict of interest.

References

1. Kataria, V.; Mehta, D.S. Multispectral harvesting rare-earth oxysulphide based highly efficient transparent luminescent solar concentrator. *J. Rare Earth* **2022**, *40*, 41–48. [CrossRef]
2. Alekhin, M.S.; Renger, J.; Kasperczyk, M.; Douissard, P.-A.; Martin, T.; Zorenko, Y.; Vasil'ev, D.A.; Stiefel, M.; Novotny, L.; Stampanoni, M. STED properties of Ce^{3+}, Tb^{3+}, and Eu^{3+} doped inorganic scintillators. *Opt. Express* **2017**, *25*, 1251–1261. [CrossRef]
3. Grigorjevaite, J.; Ezerskyte, E.; Paterek, J.; Saitzek, S.; Zabiliute-Karaliune, A.; Vitta, P.; Enseling, D.; Justel, T.; Katelnikovas, A. Luminescence and luminescence quenching of $K_2Bi(PO_4)(MoO_4):Sm^{3+}$ phosphors for horticultural and general lighting applications. *Mater. Adv.* **2020**, *1*, 1427–1438. [CrossRef]
4. Sujecki, S. Modelling and Design of Lanthanide Ion-Doped Chalcogenide Fiber Lasers: Progress towards the Practical Realization of the First MIR Chalcogenide Fiber Laser. *Fibers* **2018**, *6*, 25. [CrossRef]
5. Cheng, F.R.; Xia, Z.G.; Jing, X.P.; Wang, Z.Y. Li/Ag ratio dependent structure and upconversion photoluminescence of $Li_xAg_{1-x}Yb_{0.99}(MoO_4)_2:0.01Er^{3+}$ phosphors. *Phys. Chem. Chem. Phys.* **2015**, *17*, 3689–3696. [CrossRef]
6. Grigorjevaite, J.; Katelnikovas, A. Synthesis and optical properties investigation of blue-excitable red-emitting $K_2Bi(PO_4)(MoO_4):Pr^{3+}$ powders. *J. Mater. Res. Technol.* **2020**, *9*, 15779–15787. [CrossRef]
7. Lamon, S.; Wu, Y.; Zhang, Q.; Liu, X.; Gu, M. Nanoscale optical writing through upconversion resonance energy transfer. *Sci. Adv.* **2021**, *7*, eabe2209. [CrossRef]
8. Liu, Y.J.; Lu, Y.Q.; Yang, X.S.; Zheng, X.L.; Wen, S.H.; Wang, F.; Vidal, X.; Zhao, J.B.; Liu, D.M.; Zhou, Z.G.; et al. Amplified stimulated emission in upconversion nanoparticles for super-resolution nanoscopy. *Nature* **2017**, *543*, 229–233. [CrossRef] [PubMed]
9. Mahata, M.K.; Hofsass, H.C.; Vetter, U. Photon-Upconverting Materials: Advances and Prospects for Various Emerging Applications. In *Luminescence-An Outlook on the Phenomena and Their Applications*; InTech: Rijeka, Croatia, 2016; pp. 109–131. [CrossRef]
10. Suyver, J.F.; Aebischer, A.; Biner, D.; Gerner, P.; Grimm, J.; Heer, S.; Kramer, K.W.; Reinhard, C.; Gudel, H.U. Novel materials doped with trivalent lanthanides and transition metal ions showing near-infrared to visible photon upconversion. *Opt. Mater.* **2005**, *27*, 1111–1130. [CrossRef]
11. Giang, L.T.K.; Trejgis, K.; Marciniak, L.; Vu, N.; Minh, L.Q. Fabrication and characterization of up-converting beta-$NaYF_4:Er^{3+},Yb^{3+}$@$NaYF_4$ core-shell nanoparticles for temperature sensing applications. *Sci. Rep.* **2020**, *10*, 14672. [CrossRef]
12. Mikalauskaite, I.; Pleckaityte, G.; Skapas, M.; Zarkov, A.; Katelnikovas, A.; Beganskiene, A. Emission spectra tuning of upconverting $NaGdF_4$:20% Yb, 2% Er nanoparticles by Cr^{3+} co-doping for optical temperature sensing. *J. Lumin.* **2019**, *213*, 210–217. [CrossRef]
13. Gunaseelan, M.; Yamini, S.; Kumar, G.A.; Senthilselvan, J. Highly efficient upconversion luminescence in hexagonal $NaYF_4:Yb^{3+}$, Er^{3+} nanocrystals synthesized by a novel reverse microemulsion method. *Opt. Mater.* **2018**, *75*, 174–186. [CrossRef]
14. Ma, Y.R.; Qiu, P.S.; Xu, D.F.; Lin, J.R.; Tang, Y.X.; Wang, F.F.; He, X.Y.; Zhou, Z.Y.; Sun, N.X.; Zhang, X.Y.; et al. Controllable synthesis and upconversion luminescence of $NaYF_4:Yb^{3+}$, Er^{3+} nanocrystals. *Ceram Int.* **2015**, *41*, S713–S718. [CrossRef]
15. Li, H.; Xu, L.; Chen, G.Y. Controlled Synthesis of Monodisperse Hexagonal $NaYF_4$:Yb/Er Nanocrystals with Ultrasmall Size and Enhanced Upconversion Luminescence. *Molecules* **2017**, *22*, 2113. [CrossRef] [PubMed]
16. Kaminski, P.; Przybylska, D.; Klima, G.; Grzyb, T. Improvement in Luminescence Intensity of beta-$NaYF_4$: 18%Yb^{3+}, 2%Er^{3+}@β-$NaYF_4$ Nanoparticles as a Result of Synthesis in the Presence of Stearic Acid. *Nanomaterials* **2022**, *12*, 319. [CrossRef] [PubMed]
17. Grzyb, T. Bright and tunable up-conversion luminescence through cooperative energy transfer in Yb^{3+}, Tb^{3+} and Eu^{3+} co-doped $LaPO_4$ nanocrystals. *Rsc. Adv.* **2014**, *4*, 2590–2595. [CrossRef]
18. Neto, A.N.C.; Jr, R.T.M.; Shyichuk, A.; Paterlini, V.; Piccinelli, F.; Bettinelli, M.; Malta, O.L. Theoretical and Experimental Investigation of the $Tb^{3+} \rightarrow Eu^{3+}$ Energy Transfer Mechanisms in Cubic $A_3Tb_{0.90}Eu_{0.10}(PO_4)_3$ (A = Sr, Ba) Materials. *J. Phys. Chem. C* **2020**, *124*, 10105–10116. [CrossRef]
19. Mi, R.Y.; Chen, J.; Liu, Y.G.; Fang, M.H.; Mei, L.F.; Huang, Z.H.; Wang, B.C.; Zhaob, C.L. Luminescence and energy transfer of a color tunable phosphor: Tb^{3+} and Eu^{3+} co-doped $ScPO_4$. *Rsc. Adv.* **2016**, *6*, 28887–28894. [CrossRef]
20. Wang, B.X.; Ren, Q.; Hai, O.; Wu, X.L. Luminescence properties and energy transfer in Tb^{3+} and Eu^{3+} co-doped $Ba_2P_2O_7$ phosphors. *Rsc. Adv.* **2017**, *7*, 15222–15227. [CrossRef]
21. Wang, L.L.; Liu, Z.Y.; Chen, Z.; Zhao, D.; Qin, G.S.; Qin, W.P. Upconversion emissions from high-energy states of Eu^{3+} sensitized by Yb^{3+} and Ho^{3+} in β-$NaYF_4$ microcrystals under 980 nm excitation. *Opt Express* **2011**, *19*, 25471–25478. [CrossRef]
22. Suo, H.; Zhu, Q.; Zhang, X.; Chen, B.; Chen, J.K.; Wang, F. High-security anti-counterfeiting through upconversion luminescence. *Mater. Today Phys.* **2021**, *21*, 100520. [CrossRef]
23. Maciel, G.S.; Biswas, A.; Prasad, P.N. Infrared-to-visible Eu^{3+} energy upconversion due to cooperative energy transfer from an Yb^{3+} ion pair in a sol-gel processed multi-component silica glass. *Opt. Commun.* **2000**, *178*, 65–69. [CrossRef]
24. Grigorjevaite, J.; Katelnikovas, A. Optical spectroscopy studies of $K_2Bi(PO_4)(MoO_4)$:20%Yb^{3+},Er^{3+} phosphors for upconversion applications. *J. Lumin.* **2022**, *252*, 119384. [CrossRef]
25. Grigorjevaite, J.; Katelnikovas, A. Up-Converting $K_2Gd(PO_4)(WO_4)$:20%Yb^{3+},Ho^{3+} Phosphors for Temperature Sensing. *Materials* **2023**, *16*, 917. [CrossRef] [PubMed]

26. Grigorjevaite, J.; Katelnikovas, A. Optical Properties Investigation of Upconverting $K_2Gd(PO_4)(WO_4)$:20%Yb^{3+},Tm^{3+} Phosphors. *Materials* **2023**, *16*, 1305. [CrossRef] [PubMed]
27. Shannon, R.D. Revised Effective Ionic Radii and Systematic Studies of Interatomic Distances in Halides and Chalcogenides. *Acta Crystallogr.* **1976**, *A32*, 751–767. [CrossRef]
28. Terebilenko, K.V.; Zatovsky, I.V.; Baumer, V.N.; Slobodyanik, N.S.; Shishkin, O.V. $K_2Ho(PO_4)(WO_4)$. *Acta Crystallogr. Sect. E Struct. Rep. Online* **2008**, *64*, i75. [CrossRef] [PubMed]
29. Demesh, M.; Gorbachenya, K.; Kisel, V.; Volkova, E.; Maltsev, V.; Koporulina, E.; Dunina, E.; Kornienko, A.; Fomicheva, L.; Kuleshov, N. Transitions intensities and cross-sections of Tb^{3+} ions in $YAl_3(BO_3)_4$ crystal. *Osa Contin.* **2021**, *4*, 822–830. [CrossRef]
30. Li, Y.C.; Chang, Y.H.; Chang, Y.S.; Lin, Y.J.; Laing, C.H. Luminescence and energy transfer properties of Gd^{3+} and Tb^{3+} in $LaAlGe_2O_7$. *J. Phys. Chem. C* **2007**, *111*, 10682–10688. [CrossRef]
31. Huang, X.Y.; Li, B.; Guo, H. Highly efficient Eu^{3+}-activated $K_2Gd(WO_4)(PO_4)$ red-emitting phosphors with superior thermal stability for solid-state lighting. *Ceram Int.* **2017**, *43*, 10566–10571. [CrossRef]
32. Lakshminarayana, G.; Wagh, A.; Kamath, S.D.; Dahshan, A.; Hegazy, H.H.; Marzec, M.; Kityk, I.V.; Lee, D.E.; Yoon, J.; Park, T. Eu^{3+}-doped fluoro-telluroborate glasses as red-emitting components for W-LEDs application. *Opt. Mater.* **2020**, *99*, 109555. [CrossRef]
33. Lahoz, F.; Martin, I.R.; Mendez-Ramos, J.; Nunez, P. Dopant distribution in a Tm^{3+}-Yb^{3+} codoped silica based glass ceramic: An infrared-laser induced upconversion study. *J. Chem. Phys.* **2004**, *120*, 6180–6190. [CrossRef] [PubMed]
34. Paulose, P.I.; Jose, G.; Thomas, V.; Unnikrishnan, N.V.; Warrier, M.K.R. Sensitized fluorescence of Ce^{3+}/Mn^{2+} system in phosphate glass. *J. Phys. Chem. Solids* **2003**, *64*, 841–846. [CrossRef]
35. Grigorjevaite, J.; Katelnikovas, A. Luminescence and Luminescence Quenching of $K_2Bi(PO_4)(MoO_4)$:Eu^{3+} Phosphors with Efficiencies Close to Unity. *Acs. Appl. Mater. Inter.* **2016**, *8*, 31772–31782. [CrossRef] [PubMed]

Disclaimer/Publisher's Note: The statements, opinions and data contained in all publications are solely those of the individual author(s) and contributor(s) and not of MDPI and/or the editor(s). MDPI and/or the editor(s) disclaim responsibility for any injury to people or property resulting from any ideas, methods, instructions or products referred to in the content.